ICARUS 115, 228–249 (1995)

Surface Textural Properties of Icy Satellites: A Comparison between Europa and Rhea

D. L. DOMINGUE

Lunar and Planetary Institute, 3600 Bay Area Boulevard, Houston, Texas 77058
E-mail: domingue@lpi.jsc.nasa.gov

AND

G. W. LOCKWOOD AND D. T. THOMPSON

Lowell Observatory, 1400 West Mars Hill Road, Flagstaff, Arizona 86001

Received March 5, 1993; revised February 16, 1995

Solar phase curves for Rhea are presented using new telescopic opposition data along with Voyager imaging observations. Two viable solutions were found to Hapke's model (1986, *Icarus* 67, 264–280) which was used to describe this phase curve. The porosity derived from the model's opposition parameters show that the optically active portion of Rhea's regolith has a porosity between 80 and 95%, which is slightly lower than the porosity seen on Europa and higher than the porosity measured for the Moon using similar methods. The macroscopic roughness is comparable to that measured by Verbiscer and Veverka (1989, *Icarus* 82, 336–353) for Rhea. The single-particle scattering functions found in this study are predominantly forward scattering, which contradicts the results of Verbiscer and Veverka (1989). © 1995 Academic Press, Inc.

I. INTRODUCTION

Modeling of global surface brightness variations with viewing geometry has been applied to many of the icy satellites of the outer Solar System (Buratti 1984, 1985, Buratti and Veverka 1983, 1984, Buratti *et al.* 1988, 1990, Domingue *et al.* 1991, Helfenstein 1986, Helfenstein *et al.* 1988, Verbiscer and Veverka 1989, Veverka *et al.* 1987). As observations of planetary phase curves improve (by either increasing large phase angle coverage or more detailed measures of the opposition surge) or photometric models improve, the understanding of planetary surfaces increases. This paper first reviews, in small part, what is currently understood about the surfaces of Europa and Rhea through previous photometric analyses. New opposition data for Rhea are then presented. Finally the photometric behavior of Rhea is compared and contrasted with that of Europa. Although the surface morphologies and geological histories of Rhea and Europa are extremely different, we find that both objects have high-albedo icy surfaces exhibiting distinct, very narrow (less than one degree) opposition effects, and similar topographic textures. To account for these photometric similarities, we speculate about how the optical properties of surface water ice and frost may be affected by different icy satellite geological environments.

II. BACKGROUND

Photometric Model

Hapke's model (1986) has been used to describe the solar phase curves of many solar system objects. The parameters of this model include w, the single scattering albedo, and the opposition effect parameters B_0 (amplitude) and h (width). B_0, the opposition spike amplitude, is related to the percentage of light scattered from the surface of a particle. For $B_0 = 1$ all the light is scattered from the surface (Hapke 1986). Parameter h is a measure of the width of the opposition spike and is related to the particle size distribution and porosity within the regolith. In this analysis, we assume that the opposition effect is due to shadow-hiding rather than coherent backscatter (MacKintosh and John 1988, Hapke 1990). Using a simple method for comparing these sources of the opposition effect, Domingue (1992) showed that porosities derived from h (assuming the same particle size distribution) are similar regardless of the exact mechanism. The single-particle scattering function used was a double-lobed Henyey–Greenstein function with parameters b and c. The parameter b describes the angular width of the forward- and backscattering lobes, assumed to be equal to keep the total number of parameters in the model small. The parameter c describes the relative amplitudes of the lobes. This single-particle scattering function was chosen be-

0019-1035/95 $6.00

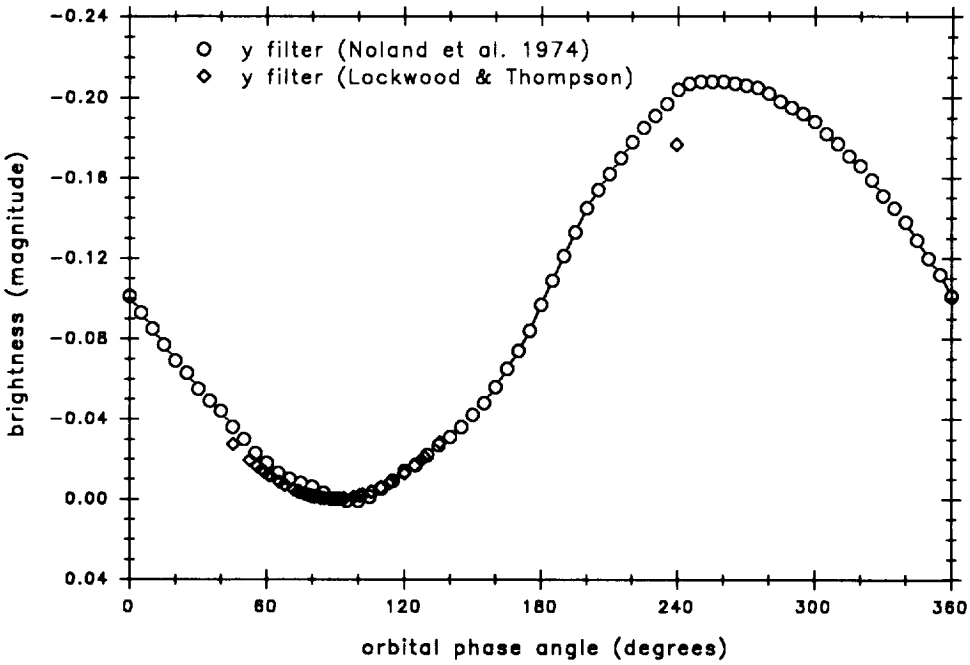

FIG. 1. Comparisons of the Rhea correction factors curves to 90° rotational phase angle from Noland *et al.* (1974) (open circles) and Lockwood and Thompson (open diamonds) for *y* filter (0.55 μm) observations.

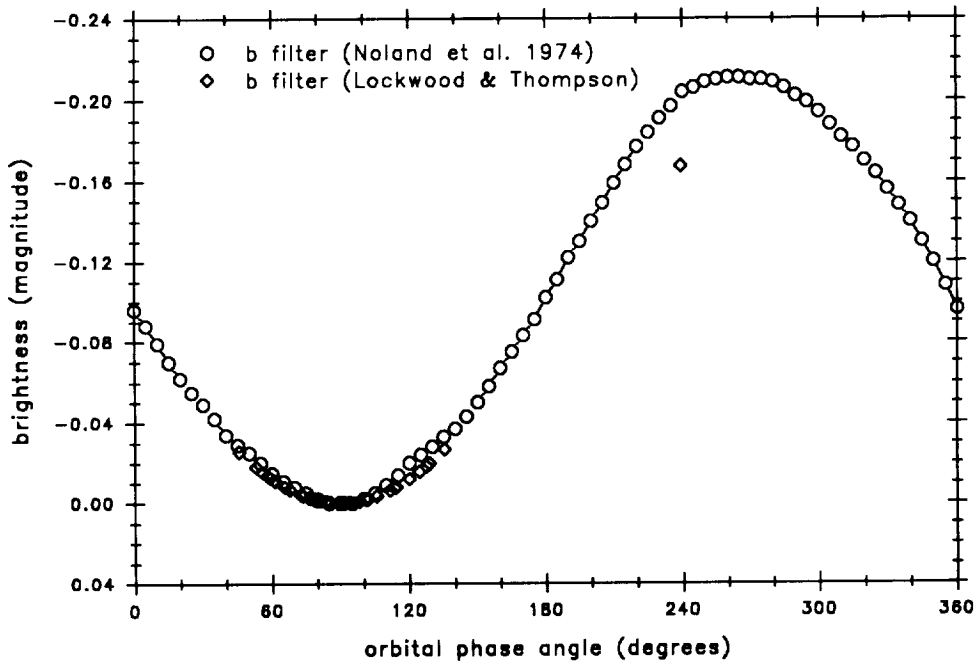

FIG. 2. Comparisons of the Rhea correction factors curves to 90° rotational phase angle from Noland *et al.* (1974) (open circles) and Lockwood and Thompson (open diamonds) for *b* filter (0.47 μm) observations.

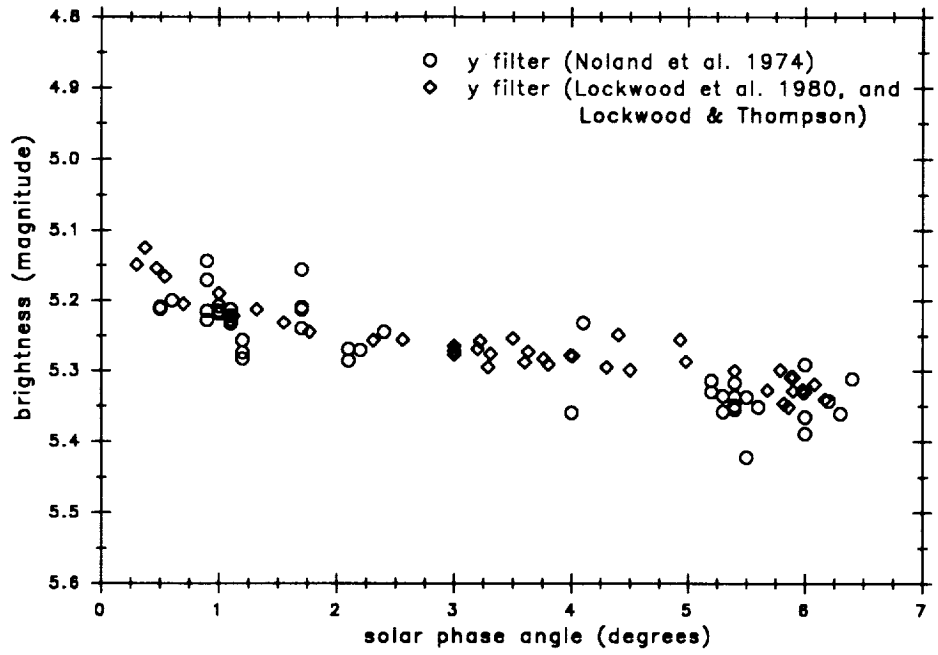

FIG. 3. Rhea solar phase curve. Comparisons of the Noland *et al.* (1974) observations (open circles) with the Lockwood *et al.* (1980) and Lockwood and Thompson (unpublished) observations (open diamonds) for the *y* filter (0.55 μm).

cause it is compatible with the single-particle scattering function used by McGuire and Hapke (1994) in their laboratory study; which will allow us to compare our results with their findings. The final Hapke parameter is $\bar{\theta}$, a measure of the average surface slope. This average is taken over a size range from a few particle diameters to the resolution limit of the Voyager images (Hapke 1984). This type of average is dominated by smaller size scales, so that $\bar{\theta}$ is predominantly a measure of the average surface tilt on millimeter to centimeter scales (Hapke 1984, Helfenstein 1988). The mathematical formulization of the model is given in Hapke (1986).

Europa Photometry

Early work by Buratti and Veverka (1983) examined the phase curve of Europa using Voyager images which covered the spectral range from 0.34 to 0.58 μm, and extended in phase angle coverage from 3° to 143°. They used an empirical lunar-Lambert phase function to describe these phase curves. Later Buratti (1985) reexamined Europa's phase curve using a radiative transfer model based on the early work of Hapke (1981, 1984) and Goguen (1981). From this study Buratti found that Europa had a more compact regolith (~65% porosity) and a more forward-scattering single-particle scattering function than the satellites Mimas, Enceladus, Rhea, and the Moon. However, this study did not include data within the opposition surge detected at less than 1° phase angle (Domingue *et al.* 1991). Photometric analysis of IUE data by Buratti *et al.* (1988) suggested porosities of 25 and 75% for the leading and trailing hemispheres, respectively. Buratti *et al.* (1988) detected no opposition surge with IUE on the leading hemisphere, but they did detect a portion of the opposition surge on the trailing hemisphere. Domingue *et al.* (1991) combined the telescopic data of Lockwood and Thompson (private communication), which describes the opposition spike in detail, with the Voyager imaging data at 0.47 and 0.55 μm. They found that both hemispheres of Europa are highly porous (≥90%) and that the single-particle scattering function has both a forward- and backscattering component, even though the backscattering component dominates.

Rhea Photometry

Using Voyager clear filter images, which covered phase angles 2° to 68°, Buratti and Veverka (1984) found phase coefficients for the satellites Rhea, Dione, Tethys, Enceladus, and Mimas that are statistically indistinguishable from previous Earth-based determinations. In their preliminary analyses of the Rhea Voyager data they did not find any clear evidence of an opposition surge (Buratti and Veverka 1984). Later Buratti (1985) applied a radiative transfer model based on the work of Hapke (1981, 1984) and Goguen (1981) to similar Voyager imaging observations of Europa, Mimas, Enceladus, and Rhea. Buratti (1985) stated that the major result of this study was that the

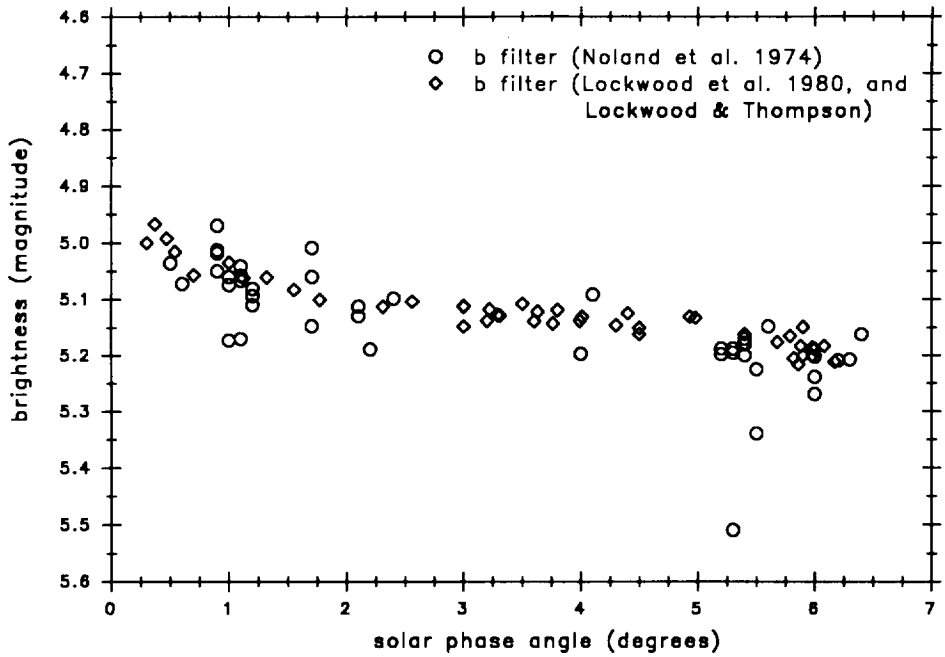

FIG. 4. Rhea solar phase curve. Comparisons of the Noland *et al.* (1974) observations (open circles) with the Lockwood *et al.* (1980) and Lockwood and Thompson (unpublished) observations (open diamonds) for the *b* filter (0.47 μm).

optically active portions of the upper regoliths of Mimas, Enceladus, and Rhea appeared to be structurally similar to the Moon's regolith. Verbiscer and Veverka (1989) expanded Buratti's (1985) work on Rhea by using an updated version of Hapke's model (Hapke 1986) and increasing the phase angle coverage by including images taken at 135° solar phase. Verbiscer and Veverka (1989) agreed with Buratti's (1985) basic conclusion that the microstructure of Rhea's regolith is similar to that of the Moon. They also found that the global large scale roughness derived from Hapke's model is similar between Rhea and the Moon. When Verbiscer and Veverka (1989) divided their data set into leading and trailing hemisphere groups, they found that the darker, trailing hemisphere was rougher than the brighter, leading hemisphere. The work done to date on Rhea has not included precise observations of the opposition surge. Verbiscer and Veverka (1989) did compare their Voyager phase curves with the Earth-based data of Noland *et al.* (1974) and found that the two phase curves were consistent within the overlapping

TABLE I
Corrections to Absolute Magnitudes for the Voyager Filters at Europa and Rhea

Filter	Hemisphere	Correction
Europa		
Clear,blue	Leading	-0.259
	Trailing	-0.317
Green,orange	Leading	-0.124
	Trailing	-0.140
Rhea		
Clear,blue	Leading	-0.200
	Trailing	-0.200
Green,orange	Leading	-0.077
	Trailing	-0.077

Note. The correction values for Europa are taken from Domingue *et al.* (1991). The corrections are (blue + correction) = clear and (orange + correction) = green.

TABLE II
Photometric Parameters

object	w	B_0	h	b	c	$\bar{\theta}$	A_p	RES
Rhea(L)								
solution 1:								
0.47μm	0.980	0.52	0.0071	-0.569	0.664	15	0.87	0.069
0.55μm	0.986	0.46	0.0071	-0.575	0.669	15	0.88	0.028
solution 2:								
0.47μm	0.970	0.45	0.0122	-0.544	0.595	14	0.84	0.068
0.55μm	0.977	0.43	0.0122	-0.547	0.596	14	0.86	0.029
Rhea(T)								
solution 1:								
0.47μm	0.927	0.50	0.0074	-0.567	0.665	16	0.72	0.097
0.55μm	0.951	0.44	0.0074	-0.567	0.677	16	0.73	0.048
solution 2:								
0.47μm	0.884	0.43	0.0122	-0.544	0.563	13	0.70	0.097
0.55μm	0.927	0.42	0.0122	-0.545	0.607	13	0.72	0.048

A_p is the physical albedo calculated from Hapke's model. Errors: $w = \pm 0.01, B_0 = \pm 0.03$, $h = \pm 0.005$, $b = c = \pm 0.01$, $\bar{\theta} = \pm 3°$.

region. However, the scatter in Noland *et al.*'s (1974) data does not clearly distinguish an opposition surge and Verbiscer and Veverka (1989) found that the scatter was too large to provide a useful independent fit of Hapke's model.

This study expands on the previous work reviewed here by combining Voyager imaging observations (which provide the large phase angle coverage) with the Earth-based observations of Lockwood *et al.* (1980) and Lockwood and Thompson (unpublished), which more accurately describe Rhea's phase curve at phase angles less than 6°, and especially within the opposition surge. Modeling the resulting phase curve using Hapke's model provides a new description of the microtexture of Rhea's regolith.

III. DATA AND ANALYTICAL METHODS

The data used in this project include telescopic observations of Rhea and disk-integrated measurements from Voyager I and II spacecraft images.

Earth-Based Observations

The new Rhea telescopic data presented here cover the leading hemisphere and were obtained between 1976 and 1986 (Lockwood *et al.* 1980, and unpublished) and are listed in Table AI of the Appendix. The table gives the universal time (UT), Julian date (JD), solar phase angle (α), rotational phase angle (ϑ), and the magnitudes $M_{0.47}$ and $M_{0.55}$, taken at 0.47 and 0.55 μm, respectively. The magnitudes $M_{0.47}$ and $M_{0.55}$ in Table AI have been corrected for rotational variation to $\vartheta = 90°$ (leading hemisphere) and $\vartheta = 270°$ (trailing hemisphere) using the correction curves in Figs. 1 and 2, normalized to a Lambertian disk of the same size at the same distance by the relationship

$$M = M_{\text{planet}} = M_{\text{sun}} - 5 \log \left(\frac{sd}{\Delta R} \right), \tag{1}$$

where s = Earth–Rhea distance = 8.539 AU, d = Sun–Rhea distance = 9.539 AU (Burns 1986), Δ = Sun–Earth distance, R = Rhea's radius = 764 km = 5.107×10^{-6} AU (Burns 1986), M_{planet} is the measured magnitude of Rhea, and M_{sun} is the magnitude of the Sun, -26.74 at 0.55 μm and -26.33 at 0.472 μm, (Allen 1973). These observations correspond closely with those made previously by Noland *et al.* (1974), as seen in Figs. 3 and 4.

In order to show that the leading hemisphere opposition parameters derived here are consistent with those for the trailing hemisphere, we also modeled the trailing hemisphere using the Voyager data coupled with Noland *et al.*'s (1974) Earth-based data. However, interpretations of the resulting opposition model parameters for the trailing hemisphere are not unique due to the scatter in the trailing hemisphere telescopic data set and should be considered with caution.

Voyager Imaging Observations

The Voyager images of Rhea taken from the Planetary Data System's CD disks (United States Geological Sur-

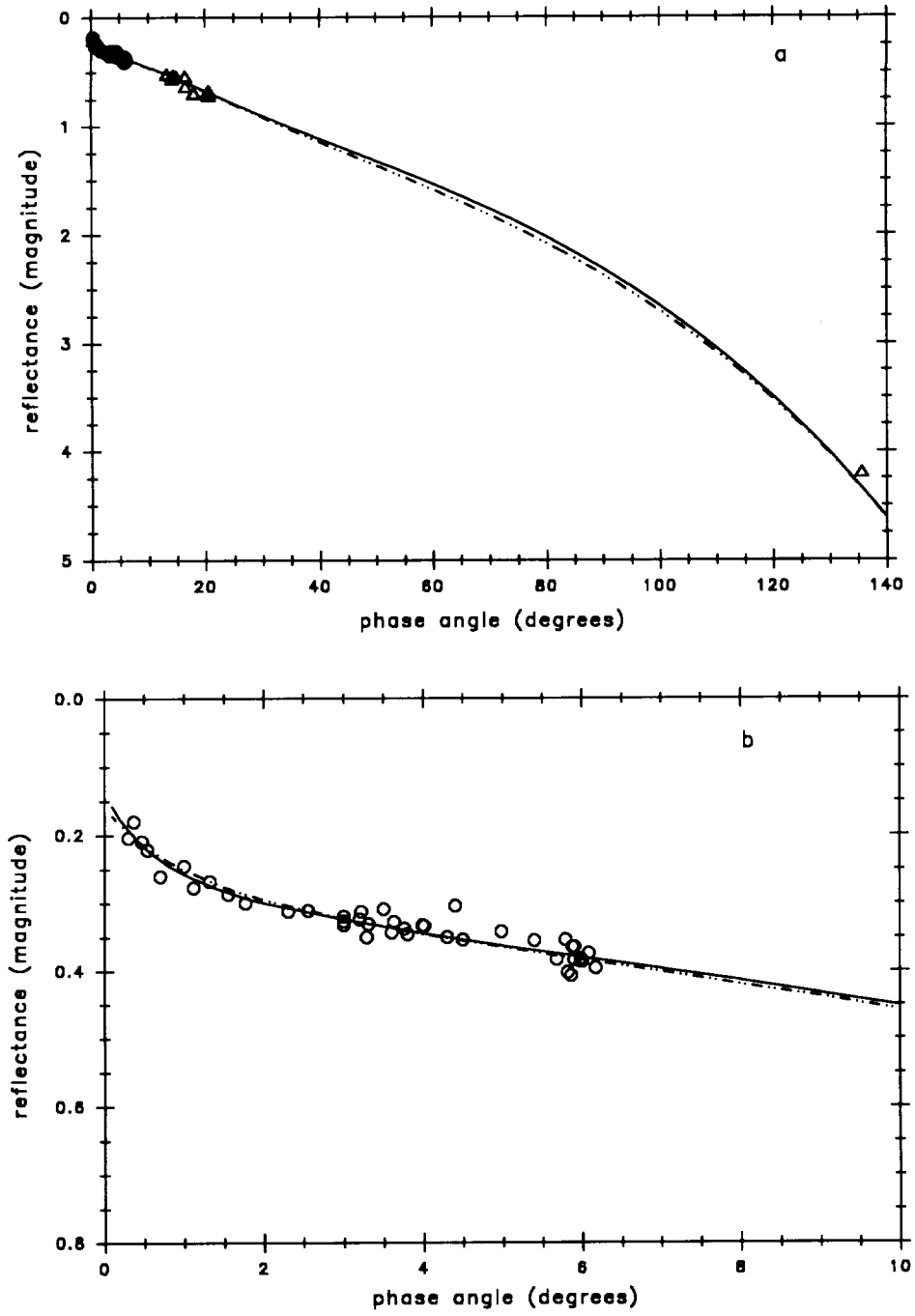

FIG. 5. Phase curve for Rhea's leading hemisphere at 0.55 μm showing (a) the full phase curve, and (b) the opposition surge. Open circles represent the telescopic data and the open triangles represent the Voyager data points. The solid line is the theoretical model using solution 1 parameter values, and the dash–dot line is the theoretical model using solution 2 parameters.

vey) are listed in Tables AII and AIII of the Appendix. These tables list the Flight Data System (FDS) count, the filter, the solar phase angle (α), the subspacecraft longitude (ϑ), the disk-integrated brightness, and the corrected disk-integrated magnitude.

The Rhea images were calibrated using the Planetary Imaging and Cartography System (PICS), a calibration software package developed by the United States Geological Survey (USGS). Disk-integrated brightness values were obtained by averaging the brightness values of the

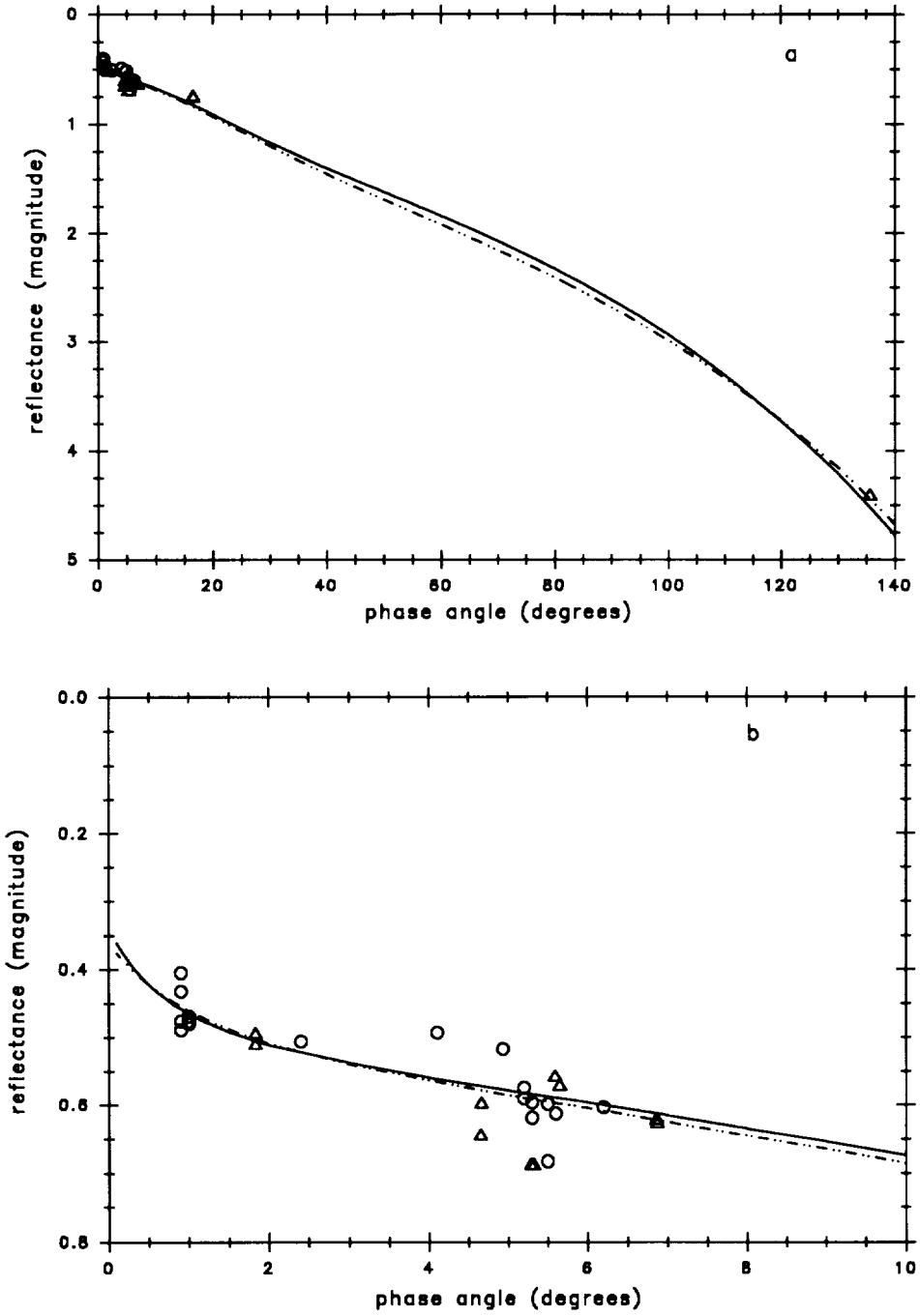

FIG. 6. Phase curve for Rhea's trailing hemisphere at 0.55 μm showing (a) the full phase curve, and (b) the opposition surge. Open circles represent the telescopic data and the open triangles represent the Voyager data points. The solid line is the theoretical model using solution 1 parameter values, and the dash–dot line is the theoretical model using solution 2 parameters.

pixels within the disk of the satellite. The uncertainty in locating the disk of the satellite in the image frame and vidicon bleeding effects result in a 1–2% uncertainty in the integral data due to this data collection technique. The overall error bars in the Voyager disk-integrated data set run between 10 and 15%.

The disk-integrated brightness (I/F) values were first converted to magnitudes (M) using the relationship $I/F = 10^{-0.4M}$. We then corrected the magnitude values using the method of Domingue *et al.* (1991). The corrections, in sequence, were as follows:

(1) Using the curve in Fig. 3 for the green and orange

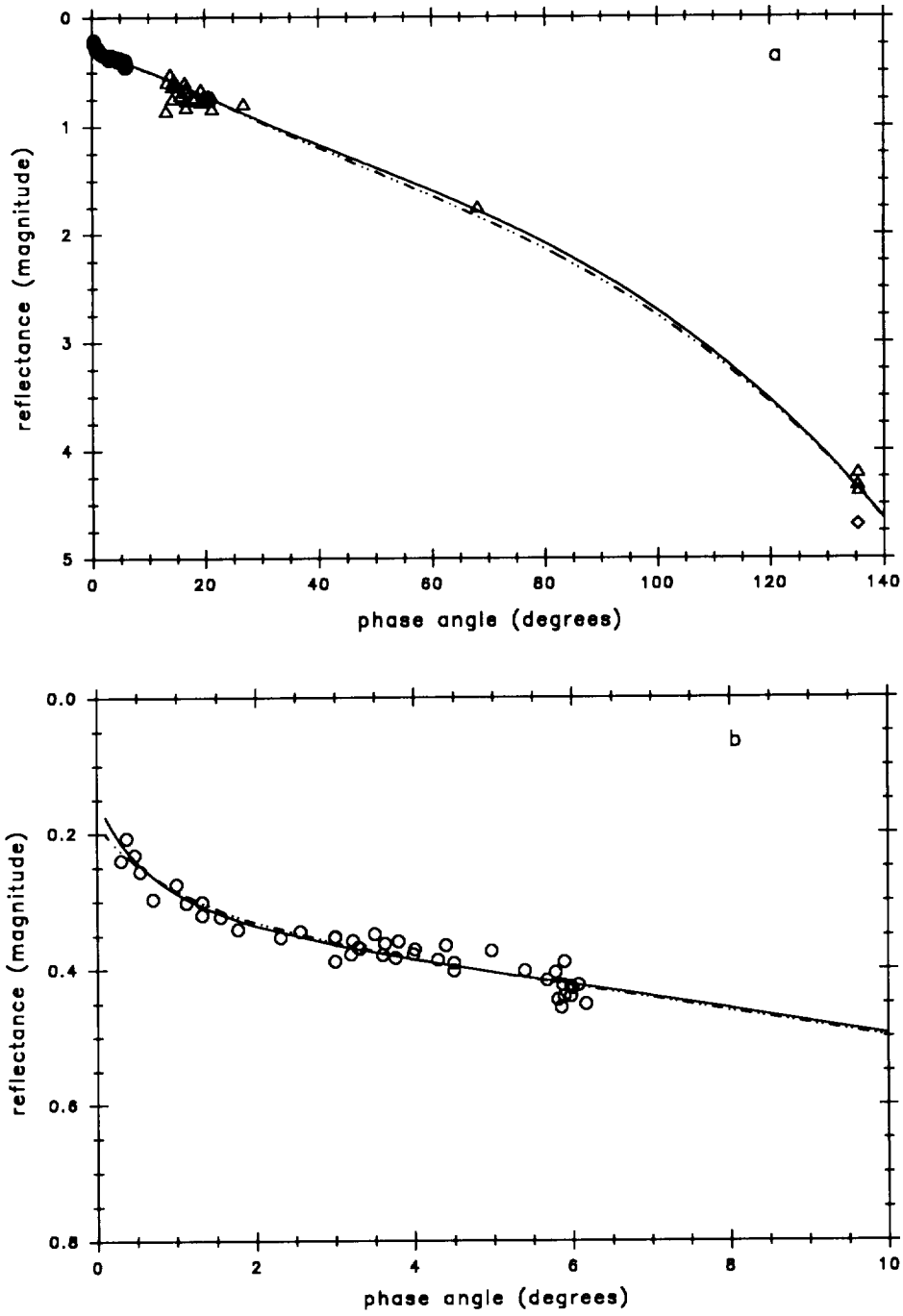

FIG. 7. Phase curve for Rhea's leading hemisphere at 0.47 μm showing (a) the full phase curve, and (b) the opposition surge. Open circles represent the telescopic data and the open triangles represent Voyager data points. The open diamond represents the data point at $\alpha = 135.35°$ extrapolated from Verbiscer and Veverka (1989). The solid line is the theoretical model using solution 1 parameter values, and the dash–dot line is the theoretical model using solution 2 parameters.

filter data, and the curve from Fig. 4 for the clear and blue filter data, we adjusted the magnitudes of all the images used to 270° rotational phase angle.

(2) The blue and orange filters have effective wavelengths within ± 0.03 μm of the clear (0.47 μm) and green (0.55 μm) filters, respectively. By comparing magnitudes at similar solar phase angles, relative corrections were found to match the blue filter data to the clear filter data, and the orange filter data to the green filter data. The data from these filters were combined in order to increase

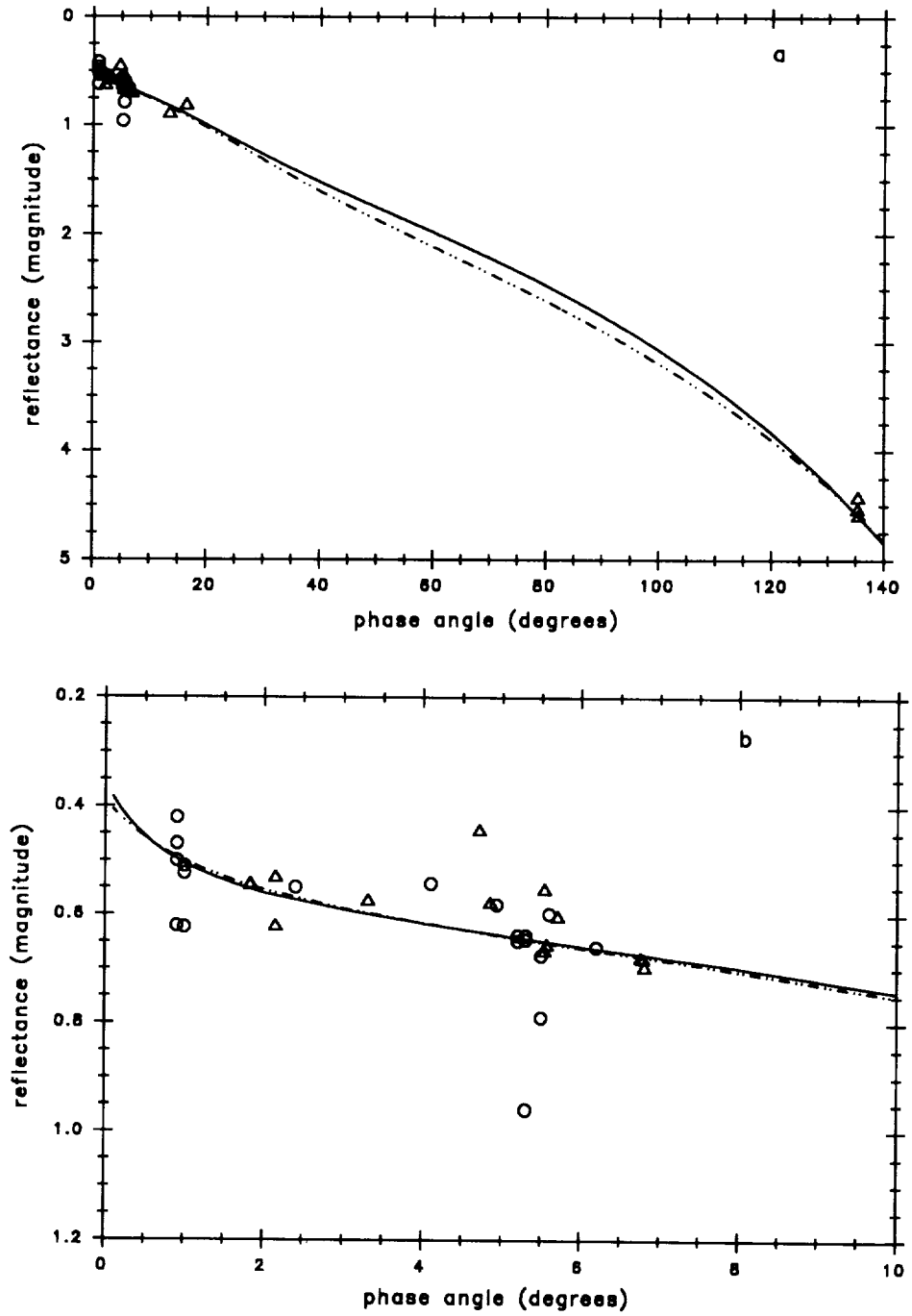

FIG. 8. Phase curve for Rhea's trailing hemisphere at 0.47 μm showing (a) the full phase curve, and (b) the opposition surge. Open circles represent the telescopic data and the open triangles represent the Voyager data points. The solid line is the theoretical model using solution 1 parameter values, and the dash–dot line is the theoretical model using solution 2 parameters.

phase angle coverage and number of observations at these two wavelengths which correspond to those of the telescopic data.

(3) We found that the narrow and wide angle camera images gave the same magnitudes at similar phase angles; thus no adjustment had to be made for differences between Voyager cameras.

(4) Likewise, Voyager I and II images gave similar results at similar phase angles; thus no relative adjustments were required for images from the two spacecraft.

TABLE III
Particle Size Distribution Function Y

Particle distribution $n(r)^a$	Function Y
$Kr^{-\beta}$: $\beta = 0$	$4/3\sqrt{3}$
1	$3/\sqrt{8\ln(r_l/r_s)}$
2	$2\sqrt{r_s/r_l}$
3	$\sqrt{2}[\ln(r_l/r_s]^{3/2}(r_s/r_l)$
4	$\sqrt{3}/\ln(r_l/r_s)$
5	$1/\sqrt{2}$

$^a n(r)dr = Kr^{-\beta}dr$ for a power law particle size distribution

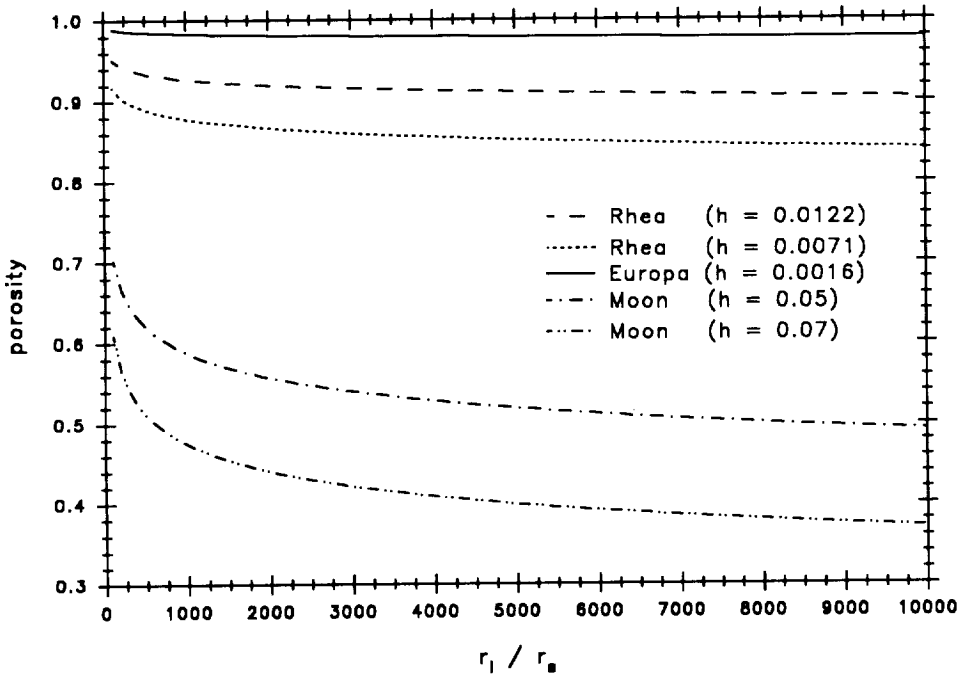

FIG. 9. A plot of the porosity function $P = \exp(-8h/3Y)$ versus the ratio of the largest to the smallest particle radii, where $Y = \sqrt{3}/\ln(r_l/r_s)$ and r_l and r_s are the largest and smallest particle radii, respectively. The solid line represents $h = 0.0016$, corresponding to the h value measured for Europa (Domingue *et al.* 1991). The dashed line represents $h = 0.0071$, corresponding to the solution 1 h value found for Rhea. The dotted line represents $h = 0.0122$, corresponding to the solution 2 h value found for Rhea. The dash–dot and dash–dot–dot lines represent h values of 0.05 and 0.07, respectively, which correspond to the h values measured for the Moon by Hapke (1986) and Helfenstein and Veverka (1987), respectively.

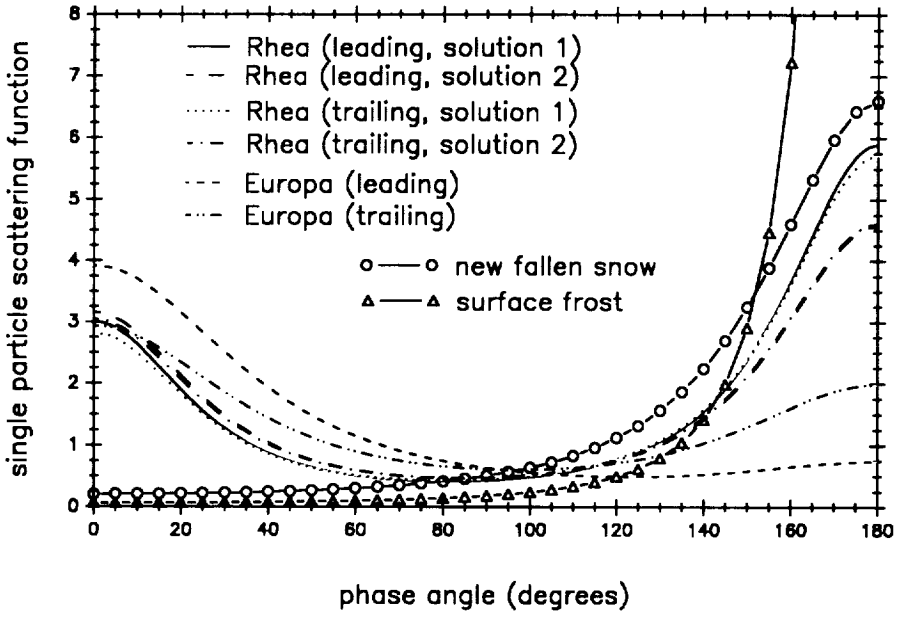

FIG. 10. The single-particle scattering function (Eq. (2)) at 0.55 μm using the (b) and (c) values listed in Table II. The solid and long-dashed lines represent Rhea's leading hemisphere (solutions 1 and 2, respectively). The dotted and dash–dot lines represent Rhea's trailing hemisphere (solutions 1 and 2, respectively). The dashed and dash–dot–dot lines represent Europa's leading and trailing hemispheres, respectively. Also included are the scattering curves for newly fallen snow in calm (circles) and terrestrial surface frost (triangles) found by Verbiscer and Veverka (1990).

(5) By comparing magnitudes at overlapping solar phase angles, a discrepancy was found between the telescopic and Voyager data sets. A correction was applied to the Voyager data to place it in agreement with the telescopic data.

(6) Finally, the leading hemisphere data were corrected to 90° rotational phase angle and separated from the trailing hemisphere data so that each hemisphere could be examined individually. Except for the images at 135° solar phase angle, the magnitudes listed for those images with ϑ between 0° and 180° have been corrected to a rotational phase angle of 90°, and those images with ϑ between 270° and 360° have been corrected to a rotational phase angle of 270°. Since the illuminated portion of the disk of the $\alpha = 135°$ images are of the leading hemisphere (Verbiscer and Veverka 1989), these images were corrected to both rotational phase angles and used in the solar phase curves of both hemispheres. This division of images into leading and trailing hemisphere does not fully separate out the two hemispheres. Due to the viewing geometries, some of the images with subspacecraft positions near 0° and 360° longitude have portions of both hemispheres illuminated. However, with the corrections for rotational phase used here the divisions are valid to first order.

The corrections applied to the Voyager data, excluding those for rotation and wavelength, are listed in Table I. The resulting magnitudes define the phase curves used in the analysis. For the clear filter images at $\alpha = 135°$, Verbiscer and Veverka (1989) corrected for rotational variations using their global albedo map. We included the resulting magnitude they found at $\alpha = 135°$ in our phase curves for comparison and completeness (differences in normalization were accounted for by setting the magnitudes of the phase curves equal at 68°).

IV. RESULTS

Photometric Model

The phase curves generated from the data discussed above were examined using Hapke's model (Hapke 1981, 1984, 1986). The single-particle scattering function used was a double-lobed Henyey–Greenstein function given by

$$P(\alpha) = \frac{(1-c)(1-b^2)}{(1+2b\cos\alpha+b^2)^{3/2}} + \frac{c(1-b^2)}{(1-2b\cos\alpha+b^2)^{3/2}}. \quad (2)$$

The parameter values for Rhea given in Table II were found using a modified least-squares grid search method (Domingue *et al.* 1991). Porosity and surface roughness are independent of wavelength. Thus, constraints were placed on the solutions such that for a particular hemi-

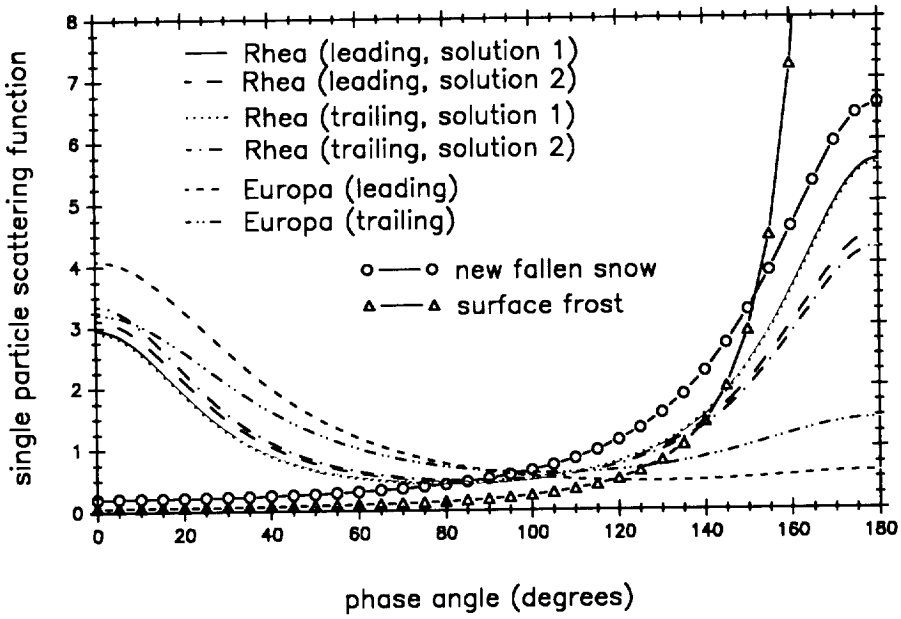

FIG. 11. The single-particle scattering function (Eq. (2)) at 0.47 μm using the b and c values listed in Table II. The solid and long-dashed lines represent Rhea's leading hemisphere (solutions 1 and 2, respectively). The dotted and dash-dot lines represent Rhea's trailing hemisphere (solution 1 and 2, respectively). The dashed and dash-dot-dot lines represent Europa's leading and trailing hemispheres, respectively. Also included are the scattering curves for newly fallen snow in calm (circles) and terrestrial surface frost (triangles) found by Verbiscer and Veverka (1990).

sphere the values of h and $\bar{\theta}$ are also independent of wavelength. All solutions with RMS residuals within 1% of the lowest RMS residual, and for whom values of h and $\bar{\theta}$ do not vary with wavelength, are considered viable solutions to the model. Two viable solutions were found which met these criteria and are listed in Table II. The residuals in Table II are defined by

$$\text{Res} = \left[\sum_{i=1}^{N} (m_{ti} - m_{di})^2\right]^{1/2}, \tag{3}$$

where m_{ti} is the calculated magnitude at phase angle α_i, and m_{di} is the observed magnitude at the same phase angle. Figures 5 through 8 compare data with theoretical curves.

Opposition Effect

The opposition effect is described by two parameters, B_0 and h. The values of B_0 for Rhea are between 0.42 and 0.52, indicating that the particles on the surface of this satellite are partially transparent, as expected from water ice or frost. Using this same model, Verbiscer and Veverka (1989) found a value of 0.656 for B_0 on Rhea. The slight differences in the values between their results and ours are due to the differences in the two data sets at small phase angles. Similarly, a low value of B_0 was found for Europa (0.5) (Domingue *et al.* 1991). Helfenstein *et al.* (1988) found a B_0 value of 0.65 for Titania and showed that Titania-like values of both B_0 and h were also consistent for other of the uranian satellites. However, Umbriel's value of B_0 (2.01) was closer to Helfenstein and Veverka's (1987) value (B_0 = 2.49) for the Moon.

The two solutions for Rhea's leading hemisphere phase curve give values of h between 0.0071 and 0.0122. The opposition data for the trailing hemisphere have too much scatter to find unique values of h and B_0. However, leading hemisphere values of h and B_0 are consistent with the trailing hemisphere data that are available, as seen in Figs. 6 and 8. Verbiscer and Veverka (1989) found a value of h = 0.08 using this same model. Once again, we attribute the different values between the two studies to differences in the data sets, especially within the opposition surge. Both hemispheres of Europa have an h value of 0.0016 (Domingue *et al.* 1991). Although Rhea's value for h is higher than Europa's, both values of h are much smaller than values found for the Moon (h = 0.05, Hapke 1986; h = 0.07, Helfenstein and Veverka 1987). Helfenstein *et al.* (1988) found h values of 0.018 and 0.061 for Titania and Umbriel. Buratti and Veverka (1984) found h values of 0.4 for Enceladus and Rhea, and a value of 0.7 for Mimas. However, the h parameter in the model used by Buratti and Veverka (1984) does not exactly correspond to h values in Hapke's 1986 model.

The parameter h is related to porosity and particle size distribution by

$$h = -\tfrac{3}{8} \ln (P) Y, \tag{4}$$

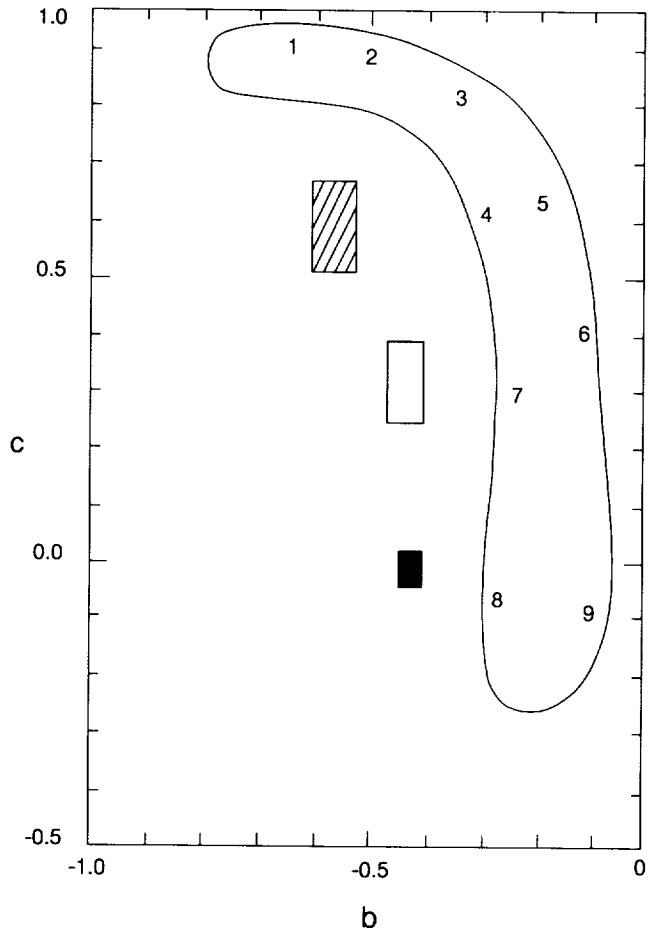

FIG. 12. A graph of b versus c adapted from McGuire and Hapke (1994) showing the scattering properties of irregular particles. Also shown are the regions of b and c values for Europa's leading (gray box) and trailing (black box) hemispheres along with Rhea's leading and trailing (hash-marked box) hemisphere. The numbers correspond to the following particle types: (1) smooth, clear, spherical, (2) low density of internal scatterers, (3) irregularly shaped, (4) rough-surfaced dielectric, (5) agglomerates, (6) smooth-surfaced metal, (7) medium density of internal scatterers, (8) high density of internal scatterers, (9) rough-surfaced metal.

where P is the porosity and Y is a function dependent on the particle size distribution. Table III, adapted from Hapke (1986), lists the functions of Y corresponding to various power-law particle size distributions. The parameters r_l and r_s are the largest and smallest particle radii, respectively. Solving this expression for porosity gives a porosity function dependent on h and an assumed particle size distribution. Figure 9 shows the porosity functions for Europa, Rhea, and the Moon using $Y = \sqrt{3}/\ln(r_l/r_s)$. This expression for Y was used since it describes the typical particle size distribution resulting from comminution processes and has been shown to characterize the lunar regolith (Bhattacharya *et al.* 1975; Hapke 1986). Regardless of the ratio of the largest to smallest particles (i.e., how well sorted the satellite surfaces are), the porosity for Europa is 95–100%, while for Rhea it is 80–95%. By comparison, the Moon's porosity is 35–70%. Europa has a consistently more porous surface than Rhea, but both satellites have surface porosities comparable to dry, powdered, terrestrial snow (Hobbs 1974). This contradicts the results and conclusions of Buratti (1985) and Verbiscer and Veverka (1989). However, their results and conclusions were based on the analysis of data sets with either no data less than 2° solar phase, or Noland *et al.*'s (1974) data which has a large degree of scatter. Buratti *et al.* (1990) found values for Irvine's compaction parameter for several of the uranian satellites (for details of this compaction parameter see Buratti 1985 and Buratti *et al.*, 1988). From this they found porosities of ~ 92% for Ariel, Titania, and Oberon, and a porosity of ~75% for Umbriel. Using a Y value of 0.25, Helfenstein *et al.*'s (1988) values of h give porosities of ~83 and ~52% for Titania and Umbriel, respectively. The exact values are a little lower than those found by Buratti *et al.* (1990), but the relative values are consistent between the two studies. Thus, the porosity of Rhea's optically active surface more closely resembles that of Titania than Umbriel. For Mimas and Enceladus, Buratti and Veverka (1984) found porosities of 20% and 10%. Buratti and Veverka (1984) also found a porosity of 10% for Rhea; however their analysis did not include the opposition data of Lockwood *et al.* (1980).

Single-Particle Scattering Function

Figures 10 and 11 display the single-particle scattering functions corresponding to 0.47 and 0.55 μm, respectively, for both solutions to Rhea's phase curve along with those of Europa. Both hemispheres of Rhea are much more strongly forward scattering than either hemisphere of Europa. Hence, we hypothesize that the particles composing Rhea's surface have fewer internal scatterers than do the particles found on the surface of Europa. The origin of these internal scatterers may involve mineral inclusions, bubbles, or microfractures in the particles.

This interpretation of b and c is substantiated by laboratory experiments involving light scattering from large irregular particles (Zerull 1976, Weiss-Wrana 1983, McGuire 1992, McGuire and Hapke 1994). These studies support each other's findings and present a consistent body of research for evaluating the physical implications of b and c derived for planetary surfaces. However, only McGuire (1992) and McGuire and Hapke (1994) examined the effects of internal scatterers and expressed the particle phase functions in the form of a double-lobed Henyey–Greenstein function, although the form of the double-lobed Henyey–Greenstein function used by McGuire and Hapke (1994) varies from that used in this analysis. McGuire and Hapke (1994) define $P(\alpha)$ by

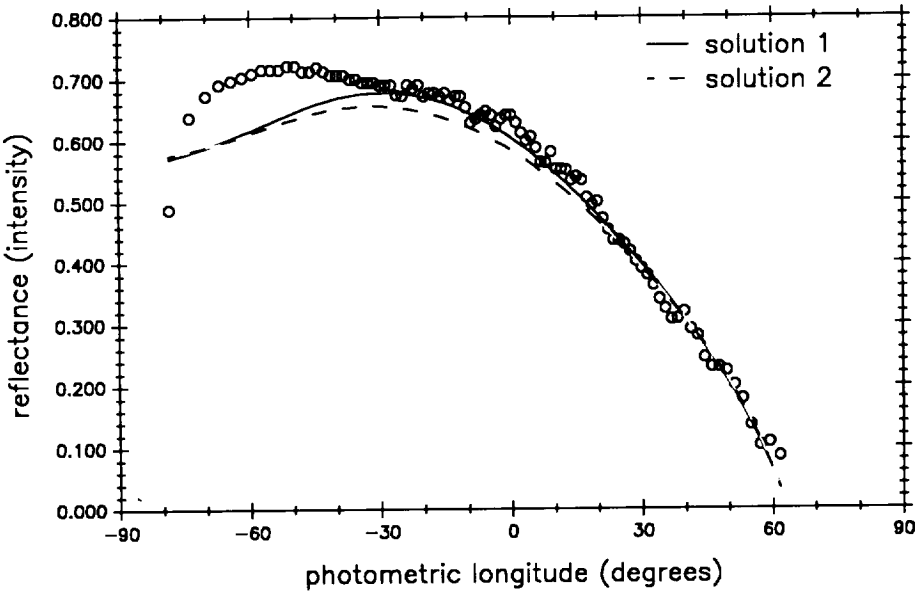

FIG. 13. Scan across the photometric equator of Voyager image 43977.14. The open circles are the data points, the solid line is the theoretical fit assuming solution 1 parameter values, and the dashed line is the theoretical fit assuming solution 2 parameter values. Both solution 1 and 2 parameters are listed in Table II. This image has a solar phase angle of 26.76°.

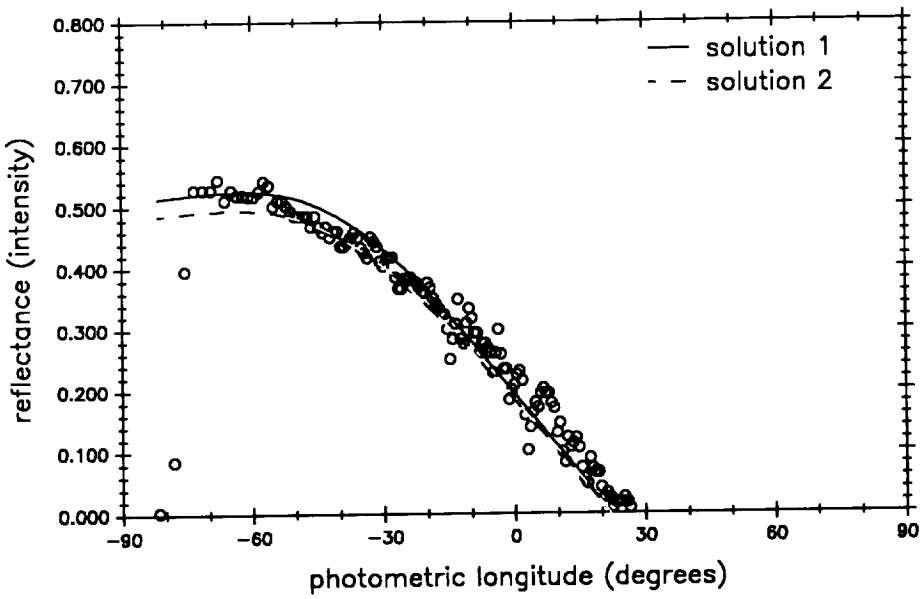

FIG. 14. Scan across the photometric equator of Voyager image 43996.08. The open circles are the data points, the solid line is the theoretical fit assuming solution 1 parameter values, and the dashed line is the theoretical fit assuming solution 2 parameter values. Both solution 1 and 2 parameters are listed in Table II. This image has a solar phase angle of 68.14°.

$$P(\alpha) = \frac{(1 - c')(1 - b^2)}{2(1 + 2b\cos\alpha + b^2)^{3/2}} + \frac{(1 + c')(1 - b^2)}{2(1 - 2b\cos\alpha + b^2)^{3/2}}. \quad (5)$$

The values of c' from Eq. (5) and the values of c from Eq. (2) are related by

$$c' = 2c - 1. \quad (6)$$

The values of b for both equations are the same.

Figure 12 is a plot of b versus c adapted from McGuire and Hapke (1994). Particles with a wide variety of mor-

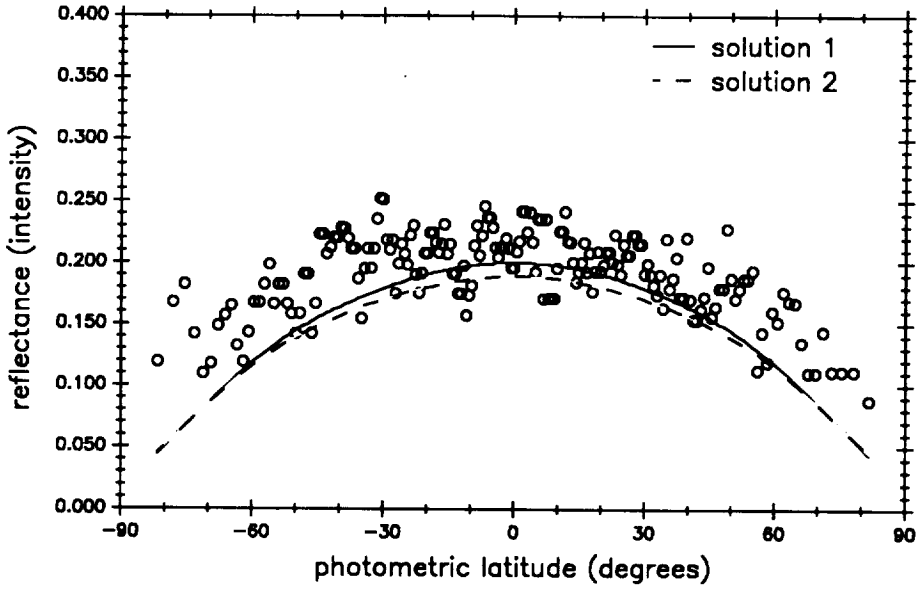

FIG. 15. Scan along the mirror meridian of Voyager image 43996.08. The open circles are the data points, the solid line is the theoretical fit assuming solution 1 parameter values, and the dashed line is the theoretical fit assuming solution 2 parameter values. Both solution 1 and 2 parameters are listed in Table II. This image has a solar phase angle of 68.14°.

phologies lie in a narrow region on this plot running from high internal scattering at one end to smooth at the other. Clear, smooth, spherical particles are strongly forward scattering and have large negative values of b and large positive values of c. Departures from these properties tends to increase the values of b and decrease the values of c. Changing the values of the single scattering albedo of a particle causes only minor changes in b and c.

As shown in the figure, b and c values for Europa are consistent with surface particles being rough-surfaced and having a large amount of internal scatterers. This agrees with the disk-resolved results of Domingue and Hapke (1992). The fact that the b and c values for Rhea (and Europa) do not lie within the region outlined by McGuire and Hapke (1994) may indicate that the surfaces of these satellites are composed of a mixture of particle types rather than a single particle type. In keeping with the highly forward-scattering nature of its single-particle phase function, both hemispheres of Rhea have b and c values which appear to correspond to rough-surfaced, irregular particles with little or no internal scatterers.

Both Buratti and Veverka (1984) and Verbiscer and Veverka (1989) used a single-parameter Henyey–Greenstein function for their single-particle scattering function and found that the scattering function was backscattering. Verbiscer (1991) used a two-term Henyey–Greenstein function in her analysis of Rhea and found that the single-particle scattering function was also backscattering. Because of the discrepancy between those results and ours, we went back and looked specifically for solutions to Hapke's model that would fit our data and also give a backscattering particle-scattering function. We did find some solutions to Hapke's model using the double-lobed Henyey–Greenstein function which had equivalent back- and forward-scattering lobes in the scattering function, but those solutions had larger RMS residuals. The error bars on b and c reflect the variations found in the different viable solution sets to Hapke's model as applied to Rhea's phase curves. We did not find any viable solutions that had a larger backscattering lobe compared to the forward-scattering lobe which met the criteria that h and $\bar{\theta}$ not vary with wavelength. This is highly unusual. The surfaces of the icy satellites, to date, have all shown backscattering particle-scattering functions. Verbiscer *et al.* (1990) have shown that in order for an icy surface to have a backscattering particle-scattering function, the frost or ice on the surface must be backscattering, unlike terrestrial frosts or snows. They have also shown that adding a darker component to provide the backscattering characteristic to an icy surface requires unrealistic values of the single scattering albedo. Therefore we interpret our results to signify a difference in the structure between the frosts on Rhea versus the other icy satellites.

Roughness

Our measured values of $\bar{\theta}$ for Rhea were between 13° ± 3° and 16° ± 3°. These values agree (within the error bars) with the global disk-integrated results ($\bar{\theta}$ = 13° ± 5°) of Verbiscer and Veverka (1989). Verification

of our disk-integrated measured value for $\bar{\theta}$ was obtained by a first-order disk-resolved analysis of several Voyager images. Figures 13 and 14 show examples of equatorial scans across the photometric equator of clear filter images taken at 68.14° and 26.76° phase angle compared to the theoretical model with the parameter values given in Table II. Figure 15 is a similar comparison of a scan along the mirror meridian of the clear filter image taken at 68.14° phase angle. Slightly better fits to the meridian scan can be obtained by increasing the value of w by ± 0.005, which is within the error bars of our solutions. Changing the value of $\bar{\theta}$ does not affect the goodness of fit to the meridian scan. Verbiscer and Veverka (1989) found evidence for a hemispherical roughness dichotomy in their more extensive disk-resolved analysis. However, neither Verbiscer and Veverka's (1989) nor our disk-integrated analyses demonstrated this dichotomy. Our values for $\bar{\theta}$ are midway between the values found by Helfenstein and Veverka (1987) for the Moon ($\bar{\theta} = 20°$) and Domingue *et al.* (1991) for Europa ($\bar{\theta} = 10°$). Our values are closer to that found for Umbriel ($\bar{\theta} = 18 \pm 3°$) by Buratti *et al.* (1990). With the exception of Triton, for which Hillier *et al.* (1991) found a $\bar{\theta}$ value of ~11°, many of the icy satellites have $\bar{\theta}$ values similar to the Moon's or higher. Helfenstein *et al.* (1988) found values of $\bar{\theta}$ for the uranian satellites ranging from 42° for Ariel to 19° for Umbriel. Buratti (1985) found a $\bar{\theta}$ value of 30° for Mimas. Therefore, Rhea's surface appears to be smoother than the majority of icy satellite surfaces, with the exceptions of Europa and Triton.

V. DISCUSSION

Spectroscopic measurements show that both Europa and Rhea have surfaces composed predominantly (>90%) of water ice and frost (Pilcher *et al.* 1972; Fink *et al.* 1973, 1976; Johnson *et al.* 1975; Pollack *et al.* 1978; Clark 1980; Clark and McCord 1980; McFadden *et al.* 1980; Clark and Owensby 1981). This conclusion supports the results of our photometric analysis, in that both satellites have: (1) high single-particle scattering albedos, as expected of water ice or frost grains, and (2) fairly small B_0 values, also as expected since neither water ice nor frost is opaque at 0.47 or 0.55 μm.

Photogeologic examinations of Voyager images indicate that Europa has a smoother surface than Rhea at kilometer scales. The $\bar{\theta}$ values for Rhea are intermediate between the Moon and Europa. The lower value of $\bar{\theta}$ for Europa than for Rhea simply indicates that the greater smoothness evident at kilometer scales also extends to millimeter and centimeter scales.

The differences between Europa's and Rhea's single-particle scattering functions are also of interest. Figures 10 and 11 show that, for both hemispheres of Europa, the single-particle scattering function is predominantly backscattering with small amounts of forward scattering. Rhea, on the other hand, is predominantly forward scattering with a backscattering lobe comparable to Europa. Figure 12 shows what this implies in terms of particle types. Essentially, particles on both satellites are rough-surfaced and irregular, but those on Europa have more internal scatterers.

An examination of Rhea's surface morphology shows that one of the major regolith-forming processes is impact gardening. The presence of a leading–trailing hemispherical albedo dichotomy similar to that seen on the Galilean satellites also suggests that its surface has been modified by micrometeoritic gardening, ion sputtering, ion implantation, or a combination of these processes. These processes have been suggested as sources for the hemispheric albedo differences on the Galilean satellites (Lane *et al.* 1981, Shoemaker and Wolfe 1982, Clark *et al.* 1983, Johnson *et al.* 1983, Clark and Lucey 1984), but would not necessarily produce different physical structures in the water ice and frost grains on Rhea and Europa. Examinations of terrestrial snow and frost show them to be strongly forward scattering (Veverka 1973, Verbiscer *et al.* 1990, Verbiscer and Veverka 1990), as seen in Figs. 10 and 11. This implies that the scattering behavior of water ice and frost dominates the single-particle scattering function measured for Rhea, but that the behavior of Europa's regolith may be strongly affected by another variable.

Geologic processes responsible for the modification of Europa's regolith are uncertain, but several have been suggested. Water volcanism (Squyres *et al.* 1983), a solid-state greenhouse (Matson and Brown 1989), micrometeorite gardening (Shoemaker and Wolfe 1982), and ion sputtering and implantation (Lane *et al.* 1981) have all been considered to have possible roles. The young surface age and high porosities deduced from the h values support the gas-driven water volcanism theory, provided the powdery "pyroclastic" ice composes a part of the resurfacing material. The high porosities could also be the result of vapor deposition from a solid-state greenhouse. Europa's hemispherical albedo dichotomy and spectral properties indicate the presence of other material besides water ice. SO_2 detected on the trailing hemisphere is also evidence for magnetospheric interactions (ion implantation) on Europa's surface (Lane *et al.* 1981). Each of these processes is capable of producing ice or frost grains with large numbers of internal scatterers. However, it is unclear that they would produce a dominantly backscattering ice or frost grain at these wavelengths. There are a few ideas which may explain these scattering curves. The differences between the scattering curves of Europa and Rhea may signify that whatever other material is present on Europa dominates the single-particle scattering function measured from disk-integrated observations. The smaller values of the single scattering albedo, w, for Europa rela-

tive to Rhea support this idea. When the results of Verbiscer *et al.*'s (1990) work is considered, this "other" component could not be substantially darker than water ice. Alternatively, the explanation for the differences in the single-particle scattering function may simply be that the structure of the frost or ice grains on Rhea are fundamentally different than those seen on other icy satellites. A final explanation may be that the observations on Europa, and even Rhea, are inadequate to measure the narrow forward-scattering lobe of water frost, as evidenced in Figs. 10 and 11. Another indication either that the data coverage needs to be expanded or that the frost/ice structures are different is the similarity in B_0 values for the two satellites. The B_0 values indicate that the material on both surfaces are more transparent than opaque, and perhaps the scattering behavior should also reflect some of this similarity.

The opposition effect parameter, h, as stated earlier, is small for both satellites as compared to the lunar value. The high porosities (>90%) implied by these values is the strongest indicator that ice and rock, even under outer solar system conditions, do not behave similarly. Rhea's high regolith porosity shows that impact-generated ice regoliths have a different texture than impact-generated rock regoliths. Chapman and McKinnon (1986) suggested that such a difference may result from a larger vapor production during impact into ice than into rock. The results from this study would support a hypothesis that the water vapor produced during impact is redeposited as a porous layer of frost. An alternative explanation for Rhea's high porosity and hemispherical dichotomy is that like Europa, there may be water volcanism occurring on the surface. However, there is no strong geological evidence for this hypothesis.

We conclude that the regoliths of both satellites are compositionally dominated by water ice and frost; however, the single-particle scattering function indicates that the structure of the ice and frosts on these two satellites may be structurally different. Data out at larger phase angles are needed to establish just how different is the scattering behavior of these two icy surfaces. The high photometrically deduced porosities indicate that frost deposition is important on both satellite surfaces. However, the different values of $\bar{\theta}$ indicate that the macroscopic texture of these frost deposits is rougher on Rhea than on Europa. This suggests that frost deposition is important on icy satellites, regardless of the geologic mechanism producing the frost.

ACKNOWLEDGMENTS

We thank the following people: Scott Murchie, Paul Helfenstein, and Anne Verbiscer for their helpful and insightful reviews, Brian Fessler and Scott Lee for their computer assistance, and Ronna Hurd for her assistance in drafting the figures. LPI Contribution No. 855.

REFERENCES

ALLEN, C. W. 1973. *Astrophysical Quantities*. Athlone Press, London.

BHATTACHARYA, S., J. GOSWAMI, D. LAL, P. PATEL, AND M. RAO 1975. Lunar regolith and gas rich meteorites: Characterization based on particle tracks and grain size distribution. *Proc. Lunar Sci. Conf. 6th*, 3509–3526.

BURATTI, B. J. 1984. Voyager disk-resolved photometry of the Saturnian satellites. *Icarus*, **59**, 392–405.

BURATTI, B. J. 1985. Application of a radiative transfer model to bright icy satellites. *Icarus* **61**, 208–217.

BURATTI, B., R. NELSON, AND A. LANE 1988. Surficial textures of the Galilean satellites. *Nature* **333**, 148–151.

BURATTI, B., AND J. VEVERKA 1983. Voyager photometry of Europa. *Icarus* **55**, 93–110.

BURATTI, B., AND J. VEVERKA 1984. Voyager photometry of Rhea, Dione, Tethys, Enceladus, and Mimas. *Icarus* **58**, 254–264.

BURATTI, B., F. WONG, AND J. MOSHER 1990. Surface properties and photometry of the uranian satellites. *Icarus*, **84**, 203–214.

BURNS, J. A. 1986. Some background about satellites. In *Satellites* (J. A. Burns and M. S. Matthews, Eds.), pp.1–38. Univ. of Arizona Press, Tucson.

CHAPMAN, C. R. AND W. B. MCKINNON 1986. Cratering of planiary satellites. In *Satellites* (J. A. Burns and M. S. Matthews, Eds.) pp. 492-580. Univ. of Arizona Press, Tucson.

CLARK, R. 1980. Ganymede,Europa, Callisto, and Saturn's Rings: Compositional Analysis from Reflectance Spectroscopy. *Icarus* **44**, 388–409.

CLARK, R. N., R. P. FANALE, AND A. P. ZENT 1983. Frost grain size metamorphism: Implications for remote sensing of planetary surfaces. *Icarus* **56**, 233–245.

CLARK, R. N., AND P. G. LUCEY 1984. Spectral properties of ce-particulate mixtures and implications for remote sensing. 1. Intimate mixtures. *J. Geophys. Res.* **89**, 6341–6348.

CLARK, R. N., AND T. B. MCCORD 1980. The Galilean satellites: New near-infrared reflectance measurements (0.65–2.5 μm) and a 0.32–5 μm summary. *Icarus* **41**, 323–339.

CLARK, R. N., AND P. D. OWENSBY 1981. The infrared spectrum of Rhea. *Icarus* **46**, 354–360.

DOMINGUE, D. 1992. A simple method for comparing shadow-hiding and coherent backscatter models of the opposition effect. *Bull. Am. Astron. Soc.* **24**(3), 958.

DOMINGUE, D., AND B. HAPKE 1992. Disk-resolved photometric analysis of Europan terrains. *Icarus* **99**, 70–81.

DOMINGUE, D. L., B. W. HAPKE, G. W. LOCKWOOD, AND D. T. THOMPSON 1991. Europa's phase curve: Implications for surface structure. *Icarus* **90**, 30–42.

FINK, U., N. H. DEKKERS, AND H. P. LARSON 1973. Infrared spectra of the Galilean satellites of Jupiter. *Astrophys. J.* **179**, L155–L159.

FINK, U., H. P. LARSON, T. N. GAUTIER III, AND R. R. TREFFERS 1976. Infrared spectra of the satellites of Saturn: Identification of water ice on Iapetus, Rhea, Dione, and Tethys. *Astrophys. J.* **207**, L63–L67.

GOGUEN, J. D. 1981. *A theoretical and experimental investigation of the photometric functions of particulate surface*. Ph.D. thesis, Cornell University, Ithaca, NY.

APPENDIX

TABLE AI
Rhea Leading Hemisphere Telescopic Observations

UT							
mo	day	yr	JD	α	ϑ	$M_{0.47}$	$M_{0.55}$
01	13	76	12790.829	0.70	113.6		0.260
02	22	76	12830.769	3.60	59.1		0.343
03	25	76	12862.684	5.90	83.5		0.384
04	03	76	12871.657	6.17	78.4		0.396
01	13	76	12790.830	0.70	113.6	0.297	
02	22	76	12830.769	3.60	59.1	0.379	
03	25	76	12862.684	5.90	83.5	0.440	
04	03	76	12871.657	6.17	78.4	0.451	
11	24	76	13106.992	5.98	91.7		0.386
12	21	76	13133.900	4.50	76.5		0.354
04	09	77	13242.664	5.86	110.0		0.407
11	24	76	13106.993	5.98	91.8	0.440	
12	21	76	13133.942	4.50	79.8	0.402	
04	09	77	13242.683	5.86	111.5	0.456	
02	13	77	13187.767	1.32	52.6		0.268
02	13	77	13187.767	1.32	52.6		0.268
02	13	77	13187.771	1.32	53.0	0.320	
02	13	77	13187.771	1.32	53.0	0.320	
12	09	77	13486.976	5.88	120.0		0.364
01	09	78	13517.936	4.01	67.8		0.334
01	18	78	13526.937	3.20	65.5		0.324
02	24	78	13563.783	1.00	124.5		0.245
03	18	78	13585.755	3.31	76.6		0.331
04	23	78	13621.644	5.82	57.8		0.402
04	28	78	13626.664	6.00	98.1		0.386
12	09	77	13486.977	5.88	120.0	0.423	
01	09	78	13517.937	4.01	67.8	0.371	
01	18	78	13526.937	3.20	65.5	0.378	
02	24	78	13563.783	1.00	124.5	0.275	
03	18	78	13585.757	3.31	76.7	0.369	
04	23	78	13621.645	5.82	57.9	0.445	
04	28	78	13626.665	6.00	98.2	0.428	
11	17	78	13830.013	5.79	85.5		0.354
12	05	78	13848.029	6.08	80.1		0.374
03	15	79	13947.793	1.55	114.3		0.287
04	06	79	13969.695	3.76	60.8		0.338

TABLE AI—*Continued*

UT							
mo	day	yr	JD	α	ϑ	$M_{0.47}$	$M_{0.55}$
11	17	78	13830.014	5.79	85.6	0.405	
12	05	78	13848.029	6.08	80.1	0.423	
03	15	79	13947.794	1.55	114.4	0.323	
04	06	79	13969.695	3.76	60.8	0.383	
12	15	79	14223.026	5.98	71.9		0.382
02	08	80	14277.941	3.63	128.8		0.328
04	16	80	14345.732	3.50	135.4		0.309
12	15	79	14223.035	5.98	72.7	0.426	
02	08	80	14277.941	3.63	128.8	0.362	
04	16	80	14345.731	3.50	135.3	0.348	
04	07	81	14701.782	1.32	55.8		0.268
05	09	81	14733.699	4.30	81.1		0.350
04	07	81	14701.782	1.32	55.8	0.301	
05	09	81	14733.699	4.30	81.1	0.386	
01	26	82	14996.044	5.68	90.5		0.383
04	13	82	15072.791	0.54	90.3		0.221
05	10	82	15099.748	3.22	79.7		0.313
05	19	82	15108.702	3.99	73.7		0.333
01	26	82	14996.045	5.68	90.6	0.416	
04	13	82	15072.792	0.54	90.4	0.256	
05	10	82	15099.749	3.22	79.7	0.358	
05	19	82	15108.702	3.99	73.7	0.378	
04	05	83	15429.858	1.77	92.0		0.300
04	18	83	15442.821	0.47	45.3		0.209
04	23	83	15447.820	0.37	84.1		0.180
05	16	83	15470.761	2.56	114.1		0.311
06	16	83	15501.705	4.98	61.3		0.342
04	05	83	15429.858	1.77	92.0	0.341	
04	18	83	15442.824	0.47	45.6	0.232	
04	23	83	15447.821	0.37	84.1	0.207	
05	16	83	15470.761	2.56	114.1	0.344	
06	16	83	15501.706	4.98	61.4	0.373	
02	06	84	15737.013	5.90	85.4		0.364
02	29	84	15759.990	5.40	105.8		0.355
04	05	84	15795.902	3.00	88.9		0.332
05	07	84	15827.795	0.30	113.2		0.204
06	03	84	15854.738	3.00	102.0		0.327
06	21	84	15872.693	4.50	93.8		0.354
02	06	84	15737.014	5.90	85.5	0.389	
02	29	84	15759.990	5.40	105.8	0.402	
04	05	84	15795.910	3.00	89.6	0.388	
05	07	84	15827.806	0.30	114.0	0.240	
06	03	84	15854.729	3.00	101.3	0.353	
06	21	84	15872.693	4.50	93.8	0.391	
04	02	85	16157.944	4.40	127.4		0.304
04	15	85	16170.874	3.29	78.1		0.350
04	24	85	16179.857	2.31	74.7		0.312
05	26	85	16211.773	1.12	100.8		0.277
06	13	85	16229.741	3.00	93.9		0.320
06	22	85	16238.695	3.80	87.7		0.346
04	02	85	16157.944	4.40	127.4	0.365	
04	15	85	16170.889	3.29	78.3	0.368	
04	24	85	16179.878	2.31	76.4	0.353	
05	26	85	16211.788	1.12	102.0	0.302	
06	13	85	16229.742	3.00	94.0	0.352	
06	22	85	16238.709	3.80	88.8	0.359	

TABLE AII
Rhea Voyager Images: Leading Hemisphere

Image FDS No.	Filter	α	(ϑ)	I/F	M	Subspacecraft longitude			
34821.10	clear			15.72		22.04	0.4092	0.7112	
34831.37	clear			18.09		47.37	0.4137	0.7314	
.49	orange			18.09		47.86	0.4767	0.6894	
.45	blue			18.09		47.70	0.4203	0.7525	
.53	green			18.09		48.02	0.4762	0.6965	
34840.24	clear			19.77		68.98	0.4258	0.7190	
34846.37	clear			20.66		84.61	0.4143	0.7568	
.49	orange			20.66		85.12	0.4781	0.7163	
.45	blue			20.66		84.95	0.4255	0.7651	
.53	green			20.66		85.30	0.4836	0.7096	
34855.23	clear			21.23		107.39	0.4225	0.7285	
.30	clear			21.23		107.70	0.3840	0.8322	
34862.43	clear			20.66		127.38	0.4211	0.7130	
.55	orange			20.66		127.88	0.4906	0.6703	
.51	blue			20.66		127.70	0.4355	0.7138	
.59	green			20.66		128.07	0.4804	0.6990	
34869.55	clear			19.29		147.88	0.4352	0.6564	
34870.02	clear			19.29		148.22	0.3910	0.7727	
34877.22	clear			16.72		170.25	0.4282	0.6379	
.30	blue			16.63		170.67	0.4272	0.6777	
.38	green			16.57		171.08	0.4850	0.6317	
34950.16	orange			14.84		6.10	0.6342	0.3204	
34963.08	clear			135.35		206.42	0.0136	4.3160	
.12	clear			135.43		206.60	0.0151	4.2044	
.20	blue			135.54		206.96	0.0134	4.3726	
.24	orange			135.60		207.15	0.0168	4.1967	
43856.54	orange			14.21		71.36	0.5718	0.5373	
.57	green			14.21		71.49	0.5491	0.5627	
43857.04	clear			14.20		71.78	0.3999	0.6306	
43863.35	blue			14.94		88.41	0.4867	0.6049	
.41	green			14.91		88.67	0.5682	0.5356	
.48	clear			14.92		88.97	0.4696	0.6207	
43880.41	blue			14.52		134.60	0.4871	0.5711	
.47	green			14.50		134.89	0.5594	0.5277	
.54	clear			14.48		135.22	0.4709	0.5847	
43888.01	blue			13.83		155.76	0.4986	0.5187	
.04	orange			13.25		155.91	0.5637	0.5136	
.07	green			13.26		156.06	0.5501	0.5219	
.14	clear			13.21		156.40	0.4577	0.5886	
43966.58	clear			16.42		1.31	0.4417	0.5921	
43967.06	orange			16.50		1.55	0.5289	0.5338	
.10	green			16.55		1.67	0.5163	0.5416	
43977.14	clear			26.76		17.93	0.3824	0.7887	
43996.08	clear			68.14		25.66	0.1581	1.7487	

TABLE AIII
Rhea Voyager Images: Trailing Hemisphere

Image FDS No.	Filter	α	Subspacecraft longitude (ϑ)	I/F	M
34884.07	clear	13.49	191.39	0.3999	0.8805
34900.02	clear	4.85	242.26	0.4913	0.5766
34903.12	clear	3.31	252.08	0.4915	0.5723
34907.36	clear	1.83	265.33	0.5052	0.5413
.44	blue	1.83	265.72	0.5219	0.5434
.48	orange	1.83	265.92	0.5792	0.5089
.52	green	1.83	266.11	0.5907	0.4934
34914.51	clear	2.15	286.19	0.5132	0.5292
.57	clear	2.15	286.19	0.4722	0.6196
34925.32	blue	5.54	312.81	0.5333	0.5509
.38	clear	5.54	313.04	0.4688	0.6535
.44	clear	5.54	313.27	0.4640	0.6648
.54	green	5.59	313.65	0.5754	0.5570
34926.02	orange	5.65	313.96	0.5651	0.5706
.10	clear	5.71	314.26	0.4931	0.6017
34963.08	clear	135.35	206.42	0.0136	4.5260
.12	clear	135.43	206.60	0.0151	4.4144
.20	blue	135.54	206.96	0.0134	4.5826
.24	orange	135.60	207.15	0.0168	4.4027
43912.45	blue	6.79	230.34	0.4623	0.6801
.48	clear	6.81	230.49	0.4460	0.6956
.54	orange	6.86	230.78	0.5422	0.6200
.57	green	6.87	230.93	0.5305	0.6252
43926.23	blue	5.29	269.26	0.4538	0.6809
.27	orange	5.32	269.44	0.5033	0.6868
.31	green	5.29	269.62	0.4949	0.6867
43937.03	clear	4.71	296.97	0.4617	0.4422
.11	orange	4.65	298.48	0.5326	0.6433
.15	green	4.66	297.46	0.5460	0.5969
43950.50	clear	6.76	329.05	0.4673	0.6781
43966.58	clear	16.42	1.31	0.4417	0.8021
43967.06	orange	16.50	1.55	0.5289	0.7498
.10	green	16.55	1.67	0.5163	0.7476

HAPKE, B. 1981. Bidirectional reflectance spectroscopy. 1. Theory. *J. Geophys. Res.* **86**, 3039–3054.

HAPKE, B. 1984. Bidirectional reflectance spectroscopy. 3. Correction for macroscopic roughness. *Icarus* **59**, 41–59.

HAPKE, B. 1986. Bidirectional reflectance spectroscopy. 4. The extinction coefficient and the opposition effect. *Icarus* **67**, 264–280.

HAPKE, B. 1990. Coherent backscatter and the radar characteristics of outer planet satellites. *Icarus* **88**, 407–417.

HELFENSTEIN, P. 1986. *Derivation and analysis of geological constraints on the emplacement and evolution of terrains on Ganymede from applied differential photometry*. Ph.D. Thesis, Brown University, Providence, RI.

HELFENSTEIN, P. 1988. The geological interpretation of photometric surface roughness. *Icarus*, **73**, 462–481.

HELFENSTEIN, P., AND J. VEVERKA 1987. Photometric properties of lunar terrains derived from Hapke's equation. *Icarus* **72**, 342–357.

HELFENSTEIN, P., J. VEVERKA, AND P. THOMAS 1988. Uranus satellites: Hapke parameters from Voyager disk-integrated photometry. *Icarus* **74**, 231–239.

HILLIER, J., P. HELFENSTEIN, A. VERBISCER, AND J. VEVERKA 1991. Voyager photometry of Triton: Haze and surface photometric propjyerties. *J. Geophys. Res.* **96**, 19203–19209.

HOBBS, P. 1974. *Ice Physics*. Clarendon Press, Oxford.

JOHNSON, R. V., L. A. SODERBLOM, J. A. MOSHER, G. H. DANIELSON, A. F. COOK, AND P. KUPFERMAN 1983. Global multispectral mosaics of the icy Galilean satellites. *J. Geophys. Res.* **88**, 5789–5805.

JOHNSON, T. V., G. J. VEEDER, AND D. L. MATSON 1975. Evidence for frost on Rhea's surface. *Icarus* **24**, 428–432.

LANE, A. L., R. M. NELSON, AND D. L. MATSON 1981. Evidence for sulfur implantation in Europa's UV absorption band. *Nature* **292**, 38–39.

LOCKWOOD, G. W., D. T. THOMPSON, AND K. LUMME 1980. A possible detection of solar variability from photometry of Io, Europa, Callisto, and Rhea, 1976–1979. *Astron. J.*, **85**, 961–967.

MACKINTOSH, F., AND S. JOHN 1988. Coherent backscattering of light in the presence of time-reversal, noninvariant and parity-violating media. *Phys. Rev.*, **B37**, 1884–1897.

MATSON, D. L., AND R. H. BROWN 1989. Solid-state greenhouses and their implications for icy satellites. *Icarus* **77**, 67–81.

MCFADDEN, L. A., J. F. BELL, AND T. B. MCCORD 1980. Visible spectral reflectance measurements (0.3–1.1 μm) of the Galilean satellites at many orbital phase angles. *Icarus* **44**, 410–430.

MCGUIRE, A. 1992. *An experimental investigation of light scattering by large irregular particles*. Ph.D. dissertation, University of Pittsburgh.

MCGUIRE, A., AND B. HAPKE 1995. An experimental study of light scattering by large, irregular particles. *Icarus* **113**, 134–155.

NOLAND, M., J. VEVERKA, D. MORRISON, D. P. CRUIKSHANK, A. R. LAZAREWICZ, N. D. MORRISON, J. L. MORRISON, J. L. ELLIOT, J. GOGUEN, AND J. A. BURNS 1974. Six-color photometry of Iapetus, Titan, Rhea, Dione, and Tethys. *Icarus* **23**, 334–354.

PILCHER, C. B., S. T. RIDGWAY, AND T. B. MCCORD 1972. Galilean satellites: Identification of water frost. *Science* **178**, 1087–1089.

POLLACK, J. B., F. C. WITTEBORN, E. F. ERICKSON, D. W. STRECKER, B. J. BALDWIN, AND T. E. BUNCH 1978. Near-infrared spectra of the Galilean satellites: Observations and compositional implications. *Icarus* **36**, 271–303.

SHOEMAKER, E. M. AND R. F. WOLFE 1982. *Satellites of Jupiter*, (D. Morrison, Ed.), pp. 277–339. Univ. of Arizona Press, Tucson.

SQUYRES, S. W., R. T. REYNOLDS, P. M. CASSEN, AND S. J. PEALE 1983. Liquid water and active resurfacing on Europa. *Nature* **301**, 225–226.

VERBISCER, A. 1991. *The photometry of icy satellite surfaces*. Ph.D. dissertation, Cornell University.

VERBISCER, A., P. HELFENSTEIN, AND J. VEVERKA 1990. Backscattering from frost on icy satellites in the outer Solar System. *Nature*, **347**, 162–164.

VERBISCER, A. J., AND J. VEVERKA 1989. Albedo dichotomy of Rhea: Hapke analysis of Voyager photometry. *Icarus* **82**, 336–353.

VERBISCER, A. J., AND J. VEVERKA 1990. Scattering properties of natural snow and frost: Comparison with icy satellite photometry. *Icarus* **88**, 418–428.

VEVERKA, J. 1973. The photometric properties of natural snow and of snow-covered planets. *Icarus* **20**, 304–310.

VEVERKA, J., P. THOMAS, P. HELFENSTEIN, R. H. BROWN, AND T. V. JOHNSON 1987. Satellites of Uranus: Disk integrated photometry from Voyager imaging observations. *J. Geophys. Res.* **92**, 14895–14904.

WEISS-WRANA, K. 1983. Optical properties of interplanetary dust: Comparison with light scattering by large meteoritic and terrestrial grains. *Astron. Astrophys.* **126**, 240–250.

ZERULL, R. 1976. Scattering measurements of dielectric and absorbing non-spherical particles. *Contrib. Atmos. Phys.* **49**, 168–188.